Astronomy & Astrophysics

New high-precision strong lensing modeling of Abell 2744

Preparing for JWST observations

P. Bergamini[1,2] , A. Acebron[1,3] , C. Grillo[1,3] , P. Rosati[4,2] , G. B. Caminha[5] , A. Mercurio[6], E. Vanzella[2] ,
G. Angora[4,6] , G. Brammer[7,8], M. Meneghetti[2] , and M. Nonino[9]

[1] Dipartimento di Fisica, Università degli Studi di Milano, Via Celoria 16, 20133 Milano, Italy
  e-mail: `pietro.bergamini@unimi.it`
[2] INAF – OAS, Osservatorio di Astrofisica e Scienza dello Spazio di Bologna, Via Gobetti 93/3, 40129 Bologna, Italy
[3] INAF – IASF Milano, Via A. Corti 12, 20133 Milano, Italy
[4] Dipartimento di Fisica e Scienze della Terra, Università degli Studi di Ferrara, Via Saragat 1, 44122 Ferrara, Italy
[5] Max-Planck-Institut für Astrophysik, Karl-Schwarzschild-Str. 1, 85748 Garching, Germany
[6] INAF – Osservatorio Astronomico di Capodimonte, Via Moiariello 16, 80131 Napoli, Italy
[7] Cosmic Dawn Center (DAWN), Jagtvej 128, 2200 Copenhagen N, Denmark
[8] Niels Bohr Institute, University of Copenhagen, Jagtvej 128, København N 2200, Denmark
[9] INAF – Osservatorio Astronomico di Trieste, Via G. B. Tiepolo 11, 34143 Trieste, Italy

ABSTRACT

We present a new strong lensing (SL) model of the *Hubble* Frontier Fields (HFF) galaxy cluster Abell 2744, at $z = 0.3072$, by exploiting archival *Hubble* Space Telescope (HST) multiband imaging and Multi Unit Spectroscopic Explorer (MUSE) follow-up spectroscopy. The lens model considers 90 spectroscopically confirmed multiple images (from 30 background sources), representing the largest secure sample for this cluster field prior to the recently acquired *James Webb* Space Telescope (JWST) observations. The inclusion of the substructures within several extended sources as model constraints allowed us to accurately characterize the inner total mass distribution of the cluster and the position of the cluster critical lines. We included the lensing contribution of 225 cluster members, 202 of which are spectroscopically confirmed. We complemented this sample with 23 photometric member galaxies that are identified with a convolution neural network methodology with a high degree of purity. We also measured the internal velocity dispersion of 85 cluster galaxies, down to $m_{F160W} = 22$, to independently estimate the role of the subhalo mass component in the lens model. We investigated the effect of the cluster environment on the total mass reconstruction of the cluster core with two different mass parameterizations. We considered the mass contribution from three external clumps, either based on previous weak lensing studies, or extended HST imaging of luminous members around the cluster core. In the latter case, the observed positions of the multiple images were better reproduced, with a remarkable accuracy of $0\farcs37$, a factor of ~2 smaller than previous lens models, which exploited the same HST and MUSE data sets. As part of this work, we developed and made publicly available a Strong Lensing Online Tool (SLOT) to exploit the predictive power and the full statistical information of this and future models, through a simple graphical interface. We plan to apply our new high-precision SL model to the first analysis of the Grism Lens-Amplified Survey from Space-JWST-Early Release Science (GLASS-JWST-ERS) program, specifically to measure the intrinsic physical properties of high-z galaxies from robust magnification maps.

Key words. gravitational lensing: strong – galaxies: clusters: general – dark matter – cosmology: observations –
galaxies: clusters: individual: Abell 2744

1. Introduction

The combination of *Hubble* Space Telescope (HST) high-resolution imaging with mainly ground-based follow-up spectroscopy of lens galaxy clusters has enabled a broad range of science cases, from the charaterization of the dark matter distribution in cluster cores (Grillo et al. 2015; Limousin et al. 2016; Cerny et al. 2018; Diego et al. 2020) to cluster physics (Bonamigo et al. 2017, 2018; Annunziatella et al. 2017; Montes 2022), from cluster galaxy evolution (Annunziatella et al. 2016; Mercurio et al. 2021) and the study of high-redshift galaxies (Coe et al. 2013; Vanzella et al. 2021; Meštrić et al. 2022) to cosmological analyses (Jullo et al. 2010; Caminha et al. 2016; Grillo et al. 2018). This has motivated numerous imaging programs with HST, such as the Cluster Lensing and Supernova

survey with *Hubble* (CLASH, Postman et al. 2012), the *Hubble* Frontier Fields program (HFF, Lotz et al. 2017), the REionization LensIng Cluster Survey (RELICS, Coe et al. 2019) and the Beyond Ultra-deep Frontier Fields And Legacy Observations (BUFFALO, Steinhardt et al. 2020) survey. In parallel, follow-up spectroscopic campaigns have allowed high-precision and accurate strong lensing (SL) mass models to be built (e.g., Grillo et al. 2016; Caminha et al. 2019; Lagattuta et al. 2019; Bergamini et al. 2021a), directly impacting the precision and accuracy of subsequent cluster lensing applications (Meneghetti et al. 2020, 2022; Grillo et al. 2018; Vanzella et al. 2021). The advent of the *James Webb* Space Telescope (JWST) will push the studies mentioned above to new frontiers. In this context, the Grism Lens-Amplified Survey from Space JWST Early Release Science program (hereafter
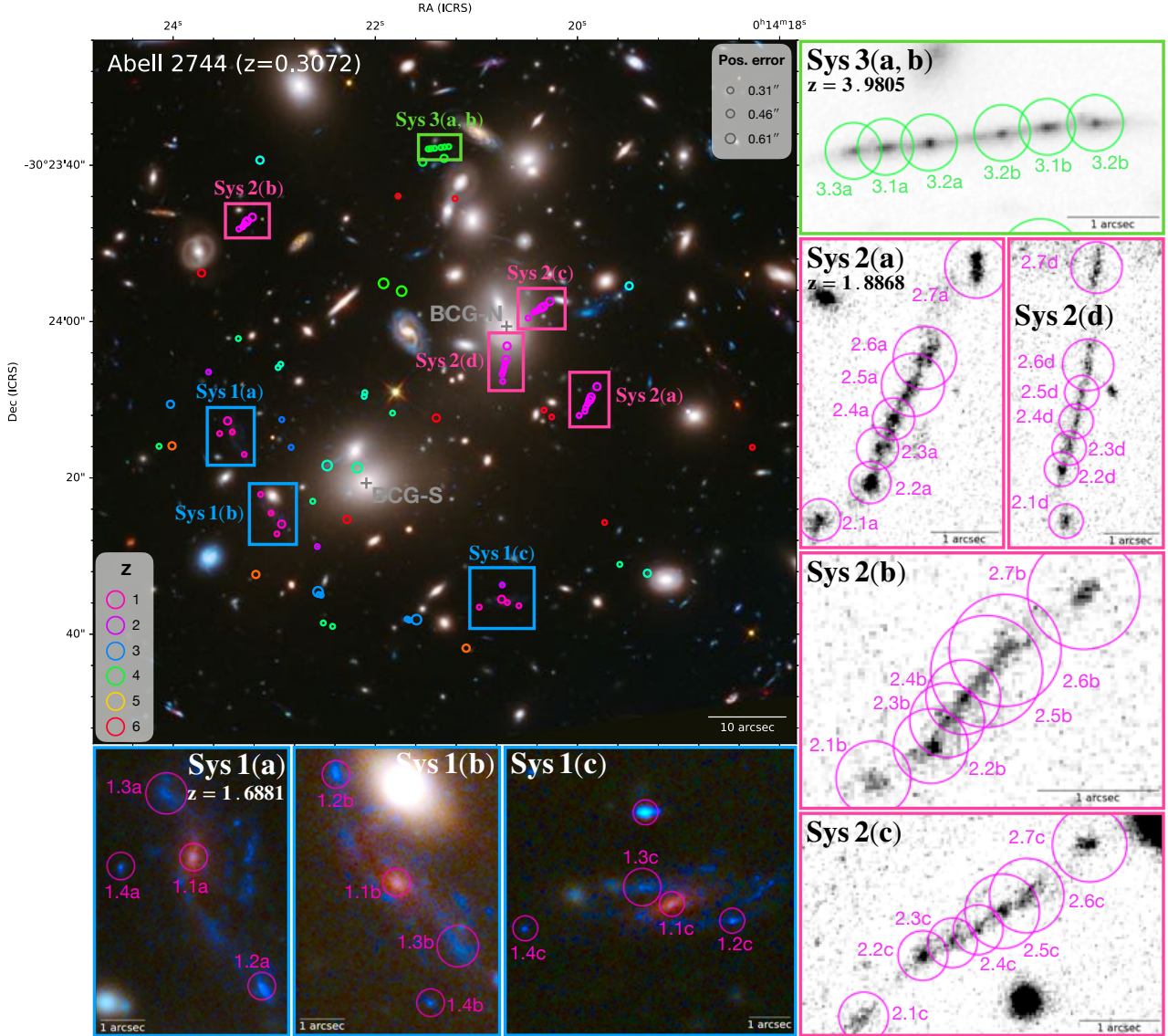
Fig. 1. Color-composite RGB image of A2744 (credits: NASA/ESA). Circles show the positions of the 90 spectroscopically confirmed multiple images included in the SL model, color-coded according to their redshift value. The size of the circle illustrates the adopted (rescaled) positional error in the modeling. Colored squares highlight the systems of multiple images for which additional lensed clumps have been identified. The two BCGs (BCG-N and BCG-S) are labeled in gray.

GLASS-JWST-ERS; JWST-ERS-1324: PI Treu, Treu et al. 2022) has recently obtained the deepest ERS data, by pointing at the galaxy cluster Abell 2744.

Abell 2744 (A2744 hereafter, see Fig. 1), at a redshift of $z = 0.3072$, is a massive, X-ray luminous, merging galaxy cluster (Allen 1998; Ebeling et al. 2010) that has been the target of extensive multiwavelength observations. The detection of a central radio halo, and a large radio-relic in the northeastern region of the cluster, led to the classification of A2744 as a recent merging system (Giovannini et al. 1999; Govoni et al. 2001). Subsequent *XMM-Newton* and *Chandra* X-ray observations, combined with rich optical spectroscopy, revealed numerous substructures in the cluster field (Kempner & David 2004; Braglia et al. 2009; Owers et al. 2011; Eckert et al. 2015). In addition, studies on the spatial distribution and kinematics of member galaxies suggested a complex internal structure in A2744 (see for instance Couch & Sharples 1987; Girardi & Mezzetti 2001; Braglia et al. 2009), showing a bimodal velocity distribution of member galax-

ies, with a high velocity-component (Owers et al. 2011). Since the detection of the first SL features in the core of the cluster (Smail et al. 1997), A2744 has also been the subject of numerous lensing analyses, from SL free-form (Lam et al. 2014; Wang et al. 2015) and parametric models (Johnson et al. 2014; Jauzac et al. 2015; Mahler et al. 2018; Richard et al. 2021, hereafter R21), to weak lensing (WL, Medezinski et al. 2016) and joint SL+WL models (Merten et al. 2011; Jauzac et al. 2016). Due to its lensing strength, A2744 was included as one of the six galaxy clusters in the HFF program with HST (Lotz et al. 2017), collecting some of the deepest high-resolution imaging of a cluster field. The HFF observations led to the identification of a very large number of photometric multiple images (up to ~180, see Jauzac et al. 2015). In particular, Zitrin et al. (2014) identified a $z_{phot} = 9.8$ triply lensed candidate system. However, the sample of secure systems remained fairly small, which has been shown to potentially introduce biases in total mass reconstructions (Grillo et al. 2015; Johnson et al. 2017). Thanks to

spectroscopic follow-up observations within the GLASS survey (Treu et al. 2015; Schmidt et al. 2014), Wang et al. (2015) provided spectroscopic redshift measurements for eight background sources. The avenue of Multi Unit Spectroscopic Explorer (MUSE, Bacon et al. 2012) follow-up observations of A2744, combined with deep HFF imaging, enabled the number of spectroscopically confirmed multiple images to significantly rise (Mahler et al. 2018; Richard et al. 2021), leading to more accurate cluster mass models.

In this work, we further exploit archival high-resolution HST imaging and MUSE spectroscopy to build an improved SL model of A2744. The new model includes the largest set of spectroscopically confirmed multiple images obtained so far in this cluster field and internal kinematics of cluster galaxies to independently constrain the subhalo total mass component. The new sample of multiple images consists of multiply lensed clumps within resolved extended sources. These additional systems are especially efficient at tightly constraining the position of the critical lines locally (see for instance Grillo et al. 2016; Bergamini et al. 2021a).

The paper is organized as follows. Section 2 describes the HST imaging and spectroscopic data sets used to develop the new lens model of A2744. In Sect. 3, we detail the adopted methodology for the SL modeling, together with the selection of the multiple images and cluster members. Our results and the Strong Lensing Online Tool (SLOT) are presented in Sects. 4 and 5, respectively, and our main conclusions are drawn in Sect. 6.

Throughout this work, we adopt a flat Lambda cold dark matter (ΛCDM) cosmology with $\Omega_m = 0.3$ and $H_0 = 70 \, \text{km s}^{-1} \, \text{Mpc}^{-1}$. Using this cosmology, a projected distance of $1''$ corresponds to a physical scale of 4.528 kpc at the A2744 redshift of $z = 0.3072$. All magnitudes are given in the AB system.

2. Data

This section presents the data sets used in this work. In Sect. 2.1 we describe the high-resolution HST imaging, while Sect. 2.2 summarizes the spectroscopic coverage of the cluster field.

2.1. HST imaging

As part of the HFF program (Proposal ID: 13495, Lotz et al. 2017), A2744 is one of the cluster fields with the deepest high-resolution observations obtained with HST. The cluster was imaged, from October 2013 to July 2014, in the optical and near-infrared with seven different bands from the Advanced Camera for Surveys (ACS; $F435W$, $F606W$, $F814W$) and the Wide Field Camera 3 (WFC3; $F105W$, $F110W$, $F140W$, $F160W$). The HFF observations, including ancillary data from previous HST programs with the same filters, were reduced with the HST science data products pipeline (Koekemoer et al. 1996). The HFF observations of A2744 were recently extended out to a larger radius, thanks to the BUFFALO survey (Steinhardt et al. 2020), which has provided shallower imaging of the outskirts of the six HFF clusters. In the following analysis, we focus on the core of the galaxy cluster and defer an extended SL analysis to a future work. We thus exploit the HFF HST mosaics with a pixel scale value of $0''03$[1].

2.2. VLT/MUSE and ancillary spectroscopy

A2744 has also been the target of extensive spectroscopic campaigns with several instruments. In particular, we used archival observations from the MUSE integral field spectrograph, mounted on the VLT (Very Large Telescope, Bacon et al. 2012), obtained within the GTO Program 094.A-0115 (PI: Richard). The data, consisting of four MUSE pointings, are described in Mahler et al. (2018), which details in Fig. 1 the exposure time within each MUSE pointing, while the reduction process is presented in R21. The MUSE data cube was reduced and analyzed following the procedure adopted in Caminha et al. (2017a,b, 2019), using the standard reduction pipeline (version 2.8.5, Weilbacher et al. 2020). In addition, we used the 'autocalibration' method and the Zurich Atmosphere Purge (ZAP, Soto et al. 2016) to improve the data reduction. The data have a full width at half maximum (FWHM) value of $0''61$. We proceeded to remeasure the redshifts of objects classified as either cluster members or multiple images in R21. The one-dimensional spectra of these objects were extracted within a $0''8$ radius circular aperture, while we applied custom apertures for faint sources, based on their estimated morphology from the HST imaging. We exploited spectral templates, as well as the identification of emission lines, to build our redshift catalogs. The reliability of each redshift measurement was then quantified with the following quality flag (QF) assignments: "insecure" (QF = 1), "likely" (QF = 2), "secure" (QF = 3), and "based on a single emission line" (QF = 9).

In addition, A2744 was targeted for 4.4h with the wide-field VIsible Multi-Object Spectrograph (VIMOS) betweeen 14 and 16 August 2004 as part of the ESO Large Program 169.A-0595 (PI: Böhringer). The spectroscopic catalog, presented in Braglia et al. (2009), includes 395 nonstellar objects with a spectroscopic confirmation. The cluster was again observed using the AAOmega multi-object spectrograph on the 3.9 m Anglo-Australian Telescope (AAT) between 12 and 18 September 2006. Combined with previous ancillary catalogs (in particular the VIMOS catalog), Owers et al. (2011) provided spectroscopic redshifts measurements for 1237 nonstellar objects within ~15′ of the cluster center, of which 343 were identified as cluster members. Finally, the GLASS HST WFC3/IR grism GO program[2] (Treu et al. 2015; Schmidt et al. 2014) provided reliable redshift measurements for 81 nonstellar objects, with a QF of probable or secure.

3. Strong lensing modeling

We developed a new lens model of A2744 using the publicly available software LensTool[3] (Kneib et al. 1996; Jullo et al. 2007; Jullo & Kneib 2009), which reconstructs the total mass distribution of a galaxy cluster by exploiting a Bayesian technique. This code was very successful at reconstructing the mass distribution of several galaxy clusters and was among the best performing codes in the Frontier Fields Lens Modeling Comparison Project (Meneghetti et al. 2017). The best-fit parameters are found by minimizing a χ^2 function, which quantifies the goodness of the lens model in reproducing the point-like positions of the observed multiple images. This statistic is defined as:

$$\chi^2(\xi) := \sum_{j=1}^{N_{\text{fam}}} \sum_{i=1}^{N_{im}^j} \left(\frac{\left\| x_{i,j}^{\text{pred}}(\xi) - x_{i,j}^{\text{obs}} \right\|}{\Delta x_{i,j}} \right)^2 , \tag{1}$$

---

[1] https://archive.stsci.edu/prepds/frontier/

[2] archive.stsci.edu/prepds/glass/
[3] https://projets.lam.fr/projects/lenstool/wiki

where $\boldsymbol{x}_{i,j}^{\text{obs}}$ represents the observed position of the ith multiple image of the jth background source (images from the same source are called a family of multiple images), and $\boldsymbol{x}_{i,j}^{\text{pred}}$, its predicted position, given the set of model free parameters $\boldsymbol{\xi}$. $\Delta x_{i,j}$ is the error associated with the position of the image.

While the best-fit model corresponds to the set of values of model free parameters for which the $\chi^2(\boldsymbol{\xi})$ assumes its minimum value, we quote the values for the parameters in the following paragraphs, and their associated errors, from the 50th, 16th, and 84th percentiles of the marginalized posterior distributions. Before sampling the posterior distributions, the initial positional uncertainty for each image, $\Delta x_{i,j}$, was rescaled so that the χ^2 value was close to the number of degrees of freedom in the model, defined as: d.o.f. $= 2 \times [N_{im}^{\text{tot}} - N_{\text{fam}}] - N_{\text{freepar}} = N_{\text{con}} - N_{\text{freepar}}$, where N_{con} and N_{freepar} are the number of model constraints and free parameters, respectively.

Moreover, we also considered and quoted the root-mean-square separation between the observed and model-predicted positions of the multiple images as another figure of merit to quantify the goodness of a lens model, which is estimated as:

$$\Delta_{\text{rms}} = \sqrt{\frac{1}{N_{im}^{\text{tot}}} \sum_{i=1}^{N_{im}^{\text{tot}}} ||\boldsymbol{\Delta}_i||^2}, \qquad (2)$$

where $\boldsymbol{\Delta}_i = \boldsymbol{x}_i^{\text{pred}} - \boldsymbol{x}_i^{\text{obs}}$ is the separation between the predicted and observed positions of the ith image.

In addition, to assess the goodness of the fit, we also considered as statistical estimator the Bayesian information criterion (BIC, Schwarz 1978) and the Akaike information criterion (AIC, Akaike 1974), which are defined as:

$$\begin{aligned} \text{BIC} &\equiv -2\ln(\mathcal{L}_{\text{max}}) + N_{\text{freepar}}\ln(N_{\text{con}}), \\ \text{AIC} &\equiv -2\ln(\mathcal{L}_{\text{max}}) + 2\,N_{\text{freepar}}, \end{aligned} \qquad (3)$$

where $\mathcal{L}_{\text{max}}$ is the maximum likelihood value.

In this section, we present the catalog of multiple images used in the model optimization, the selection and stellar kinematic measurements of member galaxies, and a summary of the adopted mass parametrization (see e.g., Bergamini et al. 2019, for a detailed description).

3.1. Multiple images

In this work, we considered previous identifications of multiple image systems presented in R21, and reanalyzed the HST multiband imaging and the MUSE data cube (see Sect. 2). The selection of secure samples of multiple images is crucial when building accurate and high-precision cluster mass models, to avoid potential biases introduced by less reliable constraints (Grillo et al. 2015; Johnson et al. 2017). Therefore, we constructed our sample by considering only secure systems that were spectroscopically confirmed by our VLT/MUSE analysis with a QF value ≥ 2. In addition, we introduced a "positional quality flag" (QP) that was then translated into different values for the initial positional uncertainty, $\Delta x_{i,j}$ in Eq. (1), assumed in the lens model (see Fig. 1). Each image was given a value of QP=1 (compact HST emission), QP=2 (diffuse or elongated HST emission), or QP=3 (MUSE-only detection).

As illustrated in Fig. 2 (bottom), the final sample of multiple image systems included in the lens model spanned a large redshift range, between $z = 1.69$ and $z = 5.73$, with a total of 90 multiple images from 30 background sources. This represents the largest spectroscopic sample of multiple images adopted so
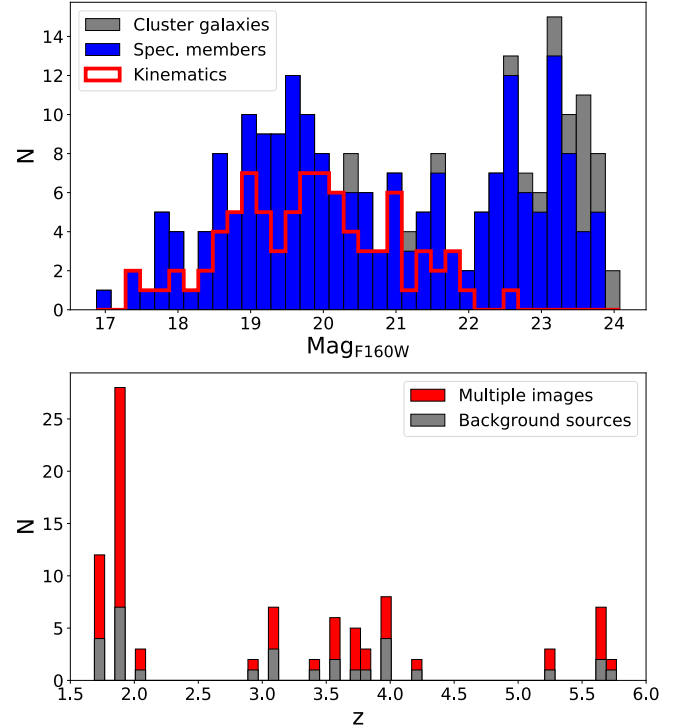

Fig. 2. Magnitude and redshift distributions of the cluster member galaxies and multiple images considered in the lens models. *Top*: distribution of cluster member galaxies as a function of their magnitudes in the HST/*F160W* filter. The photometric sample of cluster members used in our lens model is plotted in gray, with the spectroscopic members pictured in blue. Cluster members with a reliable measurement of their internal stellar velocity dispersion are highlighted in red. *Bottom*: redshift distribution of the observed 90 multiple images used to constrain the reference lens model described in this work.

far for A2744. The multiple image positions are shown in Fig. 1 and their properties are summarized in Table A.1, where the new families with respect to R21 are highlighted with a dagger symbol. The observed image positions were used as constraints in the lens model, providing in total 180 observables and 60 free parameters for the positions of the corresponding sources. All systems included in our lens model are discussed and compared below to the "gold" sample of R21 (we note that less secure candidate systems from R21 were not considered in our analysis, and are thus not discussed below). The resulting cumulative distribution of the distances of the multiple images included in the lens models is shown in Fig. 3, and is compared to that from R21. More in detail:

– Systems 1, 2, 3, 4, and 26 appear as extended images, clearly showing several resolved emission regions. In this work, we used as constraints all the multiply lensed clumps that could be securely identified. From these systems, we built a total number of 118 observational constraints, compared to the 46 from R21. This significant increase in the number of constraints in the innermost region of the cluster is illustrated in Fig. 3. An example of the new identifications is highlighted in the zoom-in insets in Fig. 1 for systems 1, 2, and 3.

– All images within Systems 6, 8, 18, 22, 34, 42, 62, 63, and 64 are included both in the catalog from R21 and ours, with no discrepancies in the redshift values.

– Systems 5, 105, 47, and 147, which form several extended images in the northernmost region of the cluster's core, were not included in our image sample. While we measured a redshift
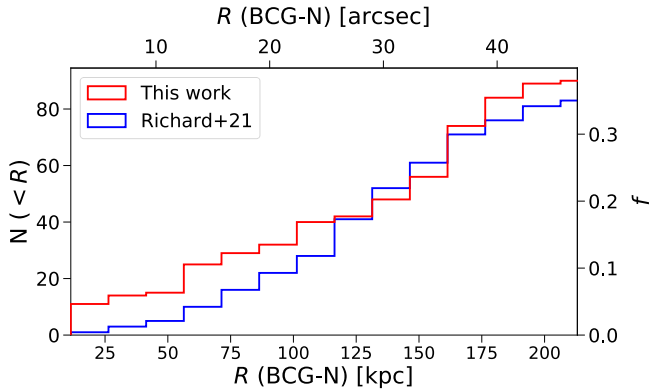
Fig. 3. Cumulative distributions of the distances of the multiple images from BCG-N of A2744. In red is the distribution of the images used as constraints in this work (90 multiple images in total) and in blue is the distribution of the images used in R21.

value in agreement with that from R21, no clear counter image positions could be identified from the HST imaging.

– Systems 10, 24, 30, 31, 41, and 61 all have a secure (QF=2 or QF=3) spectroscopic confirmation for only one of the multiple images. The remaining images have either a tentative (QF=1) or no redshift measurement. Therefore, these systems cannot be considered in the secure sample.

– System 33 is composed of three multiple images. Images 33.1a and 33.1b are in common in the two catalogs (with no redshit discrepancy), while image 33.1c is not considered in ours as no redshift measurement is possible.

– System 37 has a redshift measurement for one of the two images included in R21. This measurement was obtained with the Low Resolution Imager and Spectrograph (LRIS) at the Keck-I telescope (Mahler et al. 2018). As the redshift could not not be confirmed with MUSE, we did not include this system in our sample.

– No redshift measurement was possible for Systems 39 and 40. Thus, we removed them from our secure catalog.

3.2. Cluster members selection and stellar kinematics

Cluster member galaxies are selected based both on spectroscopic (see Sect. 2.2) and multiband HST photometric (see Sect. 2.1) information. Spectroscopically confirmed cluster members are identified as those galaxies that are brighter than $m_{F160W} = 24$ and have rest-frame ($z = 0.3072$) relative velocities within 3000 km s^{-1}, which corresponds to the redshift range [0.28–0.34]. We mainly exploited the MUSE data cube to identify 162 galaxies with a reliable redshift estimate (i.e., with a QF ≥ 2). We also included member galaxies based on spectrocpic measurements from ancillary data sets with publicly available catalogs: 32 galaxies were securely identified from the AAT/AAOmega observations (Owers et al. 2011), five objects from GLASS (Treu et al. 2015; Schmidt et al. 2014), two from the VIMOS survey (Braglia et al. 2009), and one galaxy from Couch & Sharples (1987). 28 spectroscopic galaxies from the ancillary AAT/AAOmega catalog fell outside of the HST/WFC3 field of view. We therefore adopted the following color-magnitude relation to infer the $F160W$ magnitudes: $m_{F814} - m_{F160} = 2.51 - 0.0797 \times m_{F814}$.

We completed the spectroscopic sample by selecting 23 additional photometric, bright ($m_{F160W} \leq 24$) members based on a convolution neural network (CNN) technique, which identifies

cluster members using multiband HST image cutouts together with an extensive spectroscopic coverage, as part of the CLASH-VLT program combined with MUSE archival observations (see Angora et al. 2020, for a detailed description of the method). The training set was composed of ~3300 samples, in 14 CLASH and HFF clusters (with a redshift between $z = 0.2-0.6$). When tested on the spectroscopic sample of A2744, we measured a completeness level of 88% and a high degree of purity, equal to 95%.

In summary, our final high-purity cluster member catalog, which was integrated in the following lensing analysis, consists of 225 member galaxies in total, covering an area of ~14 arcmin^2. Within this sample, 202 (or ~90%) are spectroscopically confirmed, and 23 are photometric members. We show in Fig. 2 the distribution of these cluster galaxies as a function of their magnitude in the HST/$F160W$ band, and their properties are listed in Table B.1.

As presented in Bergamini et al. (2019, 2021a), we further exploited the MUSE data cube to measure the line-of-sight stellar velocity dispersion for a large subset of cluster members. We extracted the spectra for the 162 cluster galaxies securely confirmed by the MUSE data within 0.8″ radius apertures (comparable to the MUSE PSF). Velocity dispersions were then measured using the publicly available software Penalized Pixel-Fitting method (Ppxf, Cappellari & Emsellem 2004; Cappellari 2017), over the wavelength range [3700–5700] Å. In order to exploit reliable measurements in the subsequent lensing analysis, we limited the sample to galaxies with $\langle S/N \rangle > 10$ and $\sigma_0 > 50$ km s^{-1} (see e.g., Bergamini et al. 2019, 2021a). In addition, we performed a visual inspection of the imaging and the fitted spectra, resulting in the exclusion of three faint galaxies whose spectra were contaminated by the light from the southern and northern brightest cluster galaxies (BCG-S and BCG-N, respectively). The final sample of cluster members with internal kinematics thus includes 85 galaxies, down to $m_{F160W} \sim 22$ (see Fig. 2, top). The resulting measured σ values are presented in Fig. 4, as a function of their HST/$F160W$ magnitude values.

3.3. Total mass parametrization

LensTool adopts a parametric approach, where the total mass distribution of a galaxy cluster is decomposed into the sum of several components. Extended HST imaging from the BUFFALO survey reveals several massive secondary structures in the outskirts, residing at distances between ~600−775 kpc from BCG-N, and forming multiply imaged systems in the vicinity. The massive structures, confirmed to be at the cluster's redshift, based on ancillary spectroscopy (see Sect. 2.2), can introduce a non-negligible perturbation in the positions of the multiple images in the core, and therefore impact the derived mass distribution (e.g., Acebron et al. 2017). In this work, we explore two different mass parametrizations of A2744. In the reference model, labeled LM-model, we modeled the cluster's environment as inferred from the extended BUFFALO imaging, while in the WL-model, we implemented the results from previous WL studies (Medezinski et al. 2016). The total mass distribution of the cluster is thus decomposed into the following mass contributions:

$$\phi_{tot} = \sum_{i=1}^{N_h} \phi_i^{halo} + \sum_{j=1}^{N_{bcg}} \phi_j^{BCG} + \sum_{k=1}^{N_g} \phi_k^{gal} + \sum_{l=1}^{N_s} \phi_l^{ENV}. \quad (4)$$

The first component refers to the profiles used to parameterize the cluster-scale halos of the cluster (mainly made of dark matter). The second term corresponds to the mass contribution of
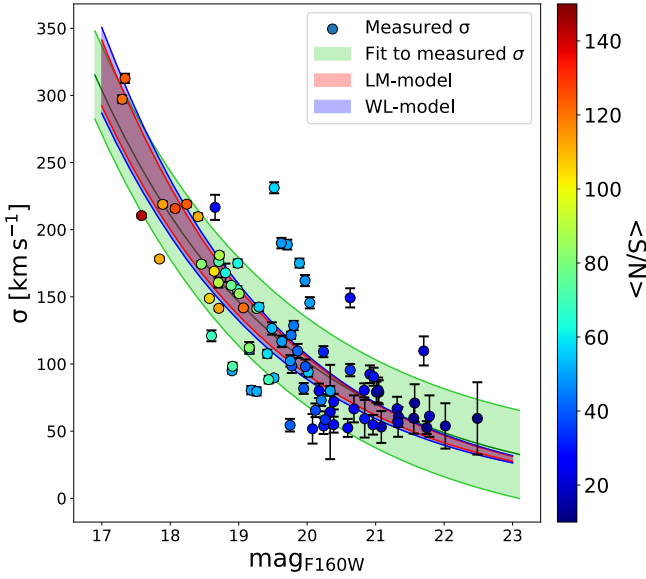
Fig. 4. Measured internal stellar velocity dispersions of 85 cluster galaxies as a function of their magnitudes in the HST/$F160W$ band are shown as filled circles, color-coded according to the mean signal-to-noise ratio of the galaxy spectra. The green line and filled area correspond to best-fit and the associated mean scatter of the $\sigma - m_{F160W}$ relation, respectively (see Sect. 3.2). The red and blue areas correspond to the 68% confidence level of the $\sigma - m_{F160W}$ relation obtained from the reference `LM-model` and the `WL-model`, respectively.

BCG-N and BCG-S in Fig. 1, which are individually optimized in the lens model. The third sum describes the mass contribution of the cluster member galaxies (the subhalo component) to the total cluster mass, modeled within scaling relations. Finally, the fourth and last component models the contribution from structures in the cluster environment (where the parametrization of the two mass models differ). A detailed description of the modeling of each component is provided below.

Both the cluster and subhalo mass component (ϕ_i^{halo}, ϕ_j^{BCG} and ϕ_k^{gal}) are described using dual pseudo-isothermal elliptical mass distributions (dPIEs, Limousin et al. 2005; Elíasdóttir et al. 2007; Bergamini et al. 2019). This profile is characterized by seven free parameters: the position (x, y); the ellipticity (defined as $e = \frac{a^2 - b^2}{a^2 + b^2}$, where a and b are the semimajor and semiminor axes of the ellipsoid, respectively); the position angle θ, computed counterclockwise from the west direction; the central velocity dispersion σ_0; the core radius r_{core}; and the truncation radius r_{cut}. We note that, instead of using σ_0, `LensTool` adopts a scaled version of this quantity, identified as σ_{LT}, such that $\sigma_{\text{LT}} = \sigma_0 \sqrt{2/3}$.

The cluster-scale component of our new lens models (ϕ_i^{halo}) is parametrized by two non-truncated elliptical dPIEs, which are centered on the BCGs, denominated BCG-N and BCG-S in Fig. 1. The halos are left free to move within a small range around the BCG positions (see Table 1).

Due to the presence of radial arcs in the vicinity of both BCGs (namely systems 2 and 4, see Fig. 1 and Table A.1), and to improve their reconstruction, the parameters describing the mass contribution, and the ellipticity, of both BCGs are individually optimized (i.e., they are modeled outside of the scaling relations). This consists of four additional free parameters for each profile.

Cluster member galaxies (ϕ_j^{gal}) are described using singular circular dPIEs whose velocity dispersions, $\sigma_{\text{LT},i}^{\text{gal}}$, and truncation radii, $r_{\text{cut},i}^{\text{gal}}$, scale with the galaxy luminosity, L_i, according to the following scaling relations (which are used to sensibly reduce the number of free parameters of the lens model):

$$\sigma_{\text{LT,i}}^{\text{gal}} = \sigma_{\text{LT}}^{\text{ref}} \left(\frac{L_i}{L_{\text{ref}}} \right)^{\alpha}, \quad r_{\text{cut},i}^{\text{gal}} = r_{\text{cut}}^{\text{ref}} \left(\frac{L_i}{L_{\text{ref}}} \right)^{\beta_{\text{cut}}}. \quad (5)$$

The reference luminosity, L_{ref}, corresponds to the BCG-N (see Fig. 1) magnitude value in the HST F160W band, $\text{mag}_{F160W}^{\text{ref}} = 17.34$. Following Bergamini et al. (2021a), we fixed $\alpha = 0.40$ and $\beta_{\text{cut}} = 0.41$. As described in Bergamini et al. (2019), these values were inferred from the measured inner stellar kinematics of 85 cluster member galaxies obtained by exploiting the MUSE data (see Sect. 3.2). A large, uniform, prior is assumed for the value of $r_{\text{cut}}^{\text{ref}}$.

As previously mentioned, the effect of the cluster environment is implemented in two different ways in our SL modeling. In our reference model, `LM-model`, we include the mass contribution from the three brightest galaxies in the northern region of the cluster (called also external clumps), which are modeled as singular isothermal sphere (SIS) profiles. Their positions are fixed to that of the light (see Table 1), while their velocity dispersion values are optimized within flat large priors that account for the galaxy and large-scale dark matter distribution (adding three free parameters in total). `LM-model` has a total number of 25 free parameters related to the mass parametrization. For the `WL-model`, the effect of the cluster environment is modeled based on the results from the WL analysis presented in Medezinski et al. (2016), using deep imaging from Subaru/Suprime-Cam. Besides the main structure associated with the cluster's core, three additional substructures were detected with a high significance value of $\gtrsim 5\sigma$. These substructures (labeled W, NE and NW in Medezinski et al. 2016 and in Fig. 5), are modeled as SIS profiles. We adopt the best-fit positions and mass parameters from Medezinski et al. (2016, Table 4), and their statistical uncertainties through large flat priors, in our lens model. Each halo thus adds three free parameters, the position, (x, y), and the velocity dispersion, σ_0. The `WL-model` has a total number of 31 free parameters related to the mass parametrization. We note that, since our models do not include multiple image constraints around these external clumps, `LensTool` determines the values of the parameters related to these profiles (i.e., the velocity dispersion and position) by quantifying their non-negligible impact on the observed multiple images in the core of the cluster.

The priors assumed for the parameters of the mass profiles included in our reference lens model, `LM-model`, are summarized in the upper part of Table 1, while the optimized values are reported in the bottom.

4. Results

The final Δ_{rms} value of our new reference lens model (`LM-model`) is $0\farcs37$, corresponding to an improvement of a factor of ~2 compared to the previous value ($0\farcs67$) obtained by R21, where a smaller sample of multiple images was used to constrain the lens model (see Table 2). In Fig. 6, we show the separations, along the x and y directions, between the observed and model predicted positions of the 90 multiple images. The figure shows that the model can accurately reproduce the observed position of the images in those cluster regions where the spatial density of image constraints is higher (more than five multiple images within $5''$). This result demonstrates that a large sample of secure multiple

Table 1. Input and output parameters of the reference model (`LM-model`) for the galaxy cluster A2744 presented in this work.

		Input parameter values and assumed priors						
		x [arcsec]	y [arcsec]	e	θ [°]	σ_{LT} [km s^{-1}]	r_{core} [arcsec]	r_{cut} [arcsec]
Cluster-scale halos	1st Cluster Halo	$-5.0 \div 5.0$	$-5.0 \div 5.0$	$0.0 \div 0.9$	$0.0 \div 180.0$	$300 \div 1500$	$0.0 \div 30.0$	2000.0
	2nd Cluster Halo	$-27.9 \div -7.9$	$-30.1 \div -10.1$	$0.0 \div 0.9$	$0.0 \div 90.0$	$300 \div 1500$	$0.0 \div 30.0$	2000.0
	1st Ext. clump	99.5	86.0	0.0	0.0	$100 \div 1500$	0.001	2000.0
	2nd Ext. clump	138.3	99.9	0.0	0.0	$100 \div 1500$	0.001	2000.0
	3rd Ext. clump	24.2	155.8	0.0	0.0	$100 \div 1500$	0.001	2000.0
Subhalos	BCG-N	0.0	0.0	$0.0 \div 0.9$	$0.0 \div 180.0$	$200 \div 400$	0.0001	$0.1 \div 50.0$
	BCG-S	-17.9	-20.0	$0.0 \div 0.9$	$0.0 \div 180.0$	$200 \div 400$	0.0001	$0.1 \div 50.0$
	Scaling relations	$N_{\rm gal} = 223$	$m_{F160W}^{\rm ref} = 17.34$	$\alpha = 0.40$		$\sigma_{LT}^{\rm ref} = 190 \div 300$	$\beta_{\rm cut} = 0.41$	$r_{\rm cut}^{\rm ref} = 0.5 \div 10.0$	$\gamma = 0.20$

		Optimized output parameters						
		x [arcsec]	y [arcsec]	e	θ [°]	σ_{LT} [km s^{-1}]	r_{core} [arcsec]	r_{cut} [arcsec]
Cluster-scale halos	1st Cluster halo	$-1.5^{+0.3}_{-0.4}$	$-0.1^{+0.8}_{-0.9}$	$0.6^{+0.1}_{-0.1}$	$90.3^{+2.5}_{-2.7}$	523^{+32}_{-32}	$6.8^{+0.8}_{-0.7}$	2000.0
	2nd Cluster halo	$-18.2^{+0.5}_{-0.5}$	$-15.7^{+0.4}_{-0.4}$	$0.4^{+0.1}_{-0.1}$	$53.3^{+2.6}_{-2.9}$	634^{+21}_{-22}	$7.6^{+0.6}_{-0.6}$	2000.0
	1st Ext. clump	99.5	86.0	0.0	0.0	201^{+124}_{-74}	0.001	2000.0
	2nd Ext. clump	138.3	99.9	0.0	0.0	933^{+32}_{-47}	0.001	2000.0
	3rd Ext. clump	24.2	155.8	0.0	0.0	776^{+30}_{-31}	0.001	2000.0
Subhalos	BCG-N	0.0	0.0	$0.3^{+0.2}_{-0.2}$	$129.6^{+20.9}_{-25.4}$	222^{+13}_{-12}	0.0001	$36.9^{+8.7}_{-10.5}$
	BCG-S	-17.9	-20.0	$0.8^{+0.1}_{-0.1}$	$26.1^{+3.7}_{-3.0}$	304^{+9}_{-11}	0.0001	$34.9^{+9.5}_{-9.6}$
	Scaling relations	$N_{\rm gal} = 223$	$m_{F160W}^{\rm ref} = 17.34$	$\alpha = 0.40$		$\sigma_{LT}^{\rm ref} = 236^{+22}_{-19}$	$\beta_{\rm cut} = 0.41$	$r_{\rm cut}^{\rm ref} = 5.8^{+2.5}_{-1.8}$	$\gamma = 0.20$

Notes. The x and y coordinates are expressed in arcseconds with respect to the position of BCG-N, at RA=3.586257, Dec = -30.400172. A single number is quoted for the fixed parameters. When a flat prior on a free parameter is considered, the boundaries of the prior separated by the $\div$ symbol are reported. The number of galaxies optimized through the scaling relations ($N_{\rm gal}$), and the reference magnitude ($m_{F160W}^{\rm ref}$) are also reported. We provide the input (top) and optimized (bottom) values of the output parameters of the reference lens model. For each free parameter, we quote the median, the 16th, and 84th percentiles of the posterior distribution.
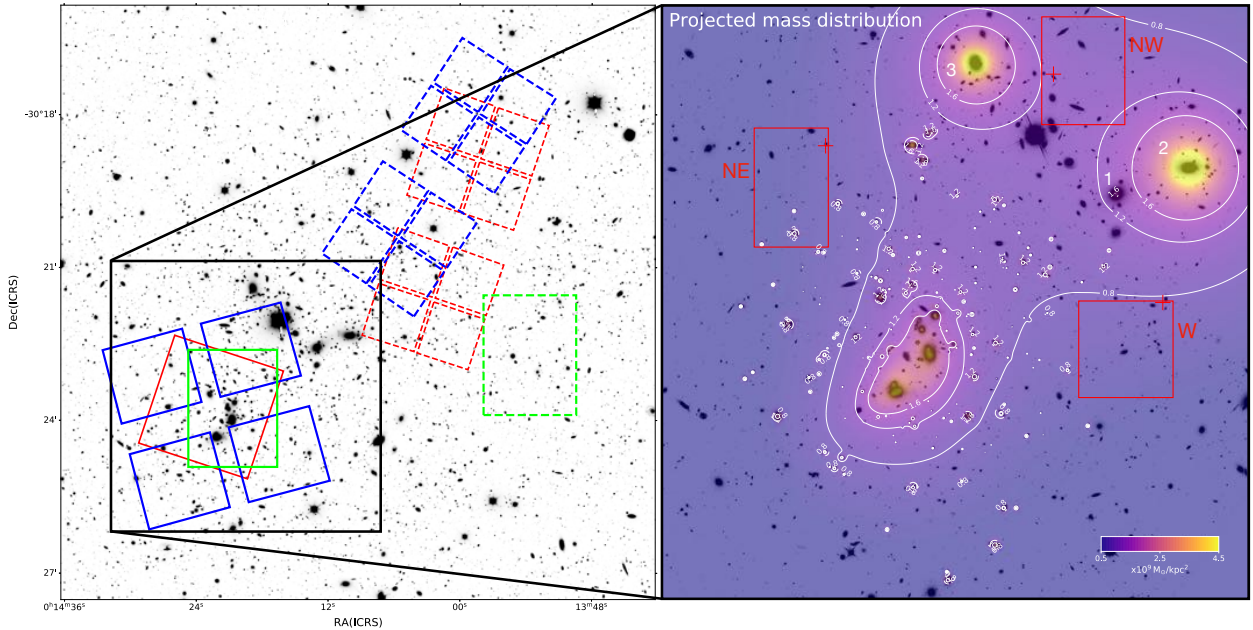

Fig. 5. Projected total mass density distribution of the galaxy cluster A2744 obtained from the `LM-model`. *Left*: Magellan R-band imaging of A2744 with the JWST footprints from the GLASS-JWST-ERS program, as also shown in Fig. 1 from Treu et al. (2022). In red and blue, we show the footprints of the NIRISS and NIRSpec pointings, respectively, while in green we plot the HFF central pointing of the cluster and the parallel field (dashed). Dashed lines correspond to parallel NIRCam pointings. *Right*: total projected mass distribution obtained from the best-fit `LM-model`, in units of $10^9\,M_\odot\,{\rm kpc}^{-2}$, overlaid on the HST/$F814W$ image. Isodensity contours corresponding to $[0.8, 1.2, 1.6] \times 10^9\,M_\odot/{\rm kpc}^2$ are plotted in white. The red rectangles indicate the assumed priors for the positions of the three WL clumps from Medezinski et al. (2016), while the red crosses show the obtained best-fit positions. The numbers 1, 2, and 3 refer to the first, second, and third external clumps (see Table 1).

images, including resolved substructures within extended images (e.g., see the cutouts in Fig. 1), and distributed all around the cluster field, is an important ingredient to develop high-precision cluster SL models (see also Grillo et al. 2016; Bergamini et al. 2021b; Pignataro et al. 2021; Diego et al. 2022).

On the other hand, the optimization of the `WL-model`, which includes the three WL halos, leads to a $\Delta_{\rm rms}$ value of $0\overset{''}{.}44$, which is significantly larger than our reference model. This underscores the better ability of the light-traces-mass approach in reproducing the mass distribution of the external

Table 2. Comparison between our new lens model for A2744 and the one from R21.

Comparison between published lens models			
Model	N_{images}	N_{sources}	Δ_{rms} [″]
This work	90	30	0.37
R21	83	29	0.67

Notes. N_{images} is the number of multiple image used as model constraints, N_{sources} is the number of background sources, and Δ_{rms} [″] is the total root-mean-square displacement between the observed and predicted image positions (see Eq. (2)).

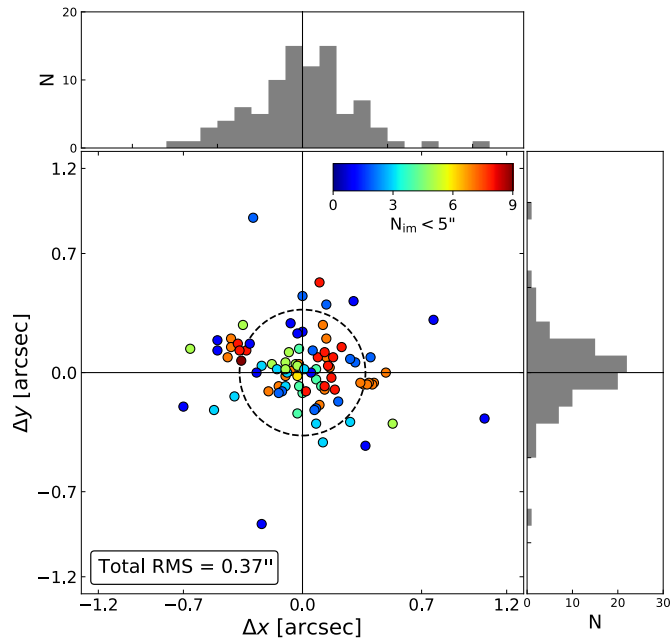**Fig. 6.** Displacements $\boldsymbol{\Delta}_i$ (see Eq. (2)) along the x and y directions of the 90 observed multiple images used to optimize the reference lens model described in this work, color-coded according to the spatial density of the images within 5″. The dashed black circle indicates the total Δ_{rms} value of 0″.37. The histograms show the displacement distribution along each direction, also illustrating the goodness of the model.

region of the cluster. This result is also supported by the lower BIC and AIC (see Eq. (3)) values for the `LM-Model` (BIC= 174, AIC=104) with respect to the `WL-Model` (BIC=231, AIC=145). As typically done in previous SL studies (see e.g., Caminha et al. 2019; Bergamini et al. 2019; Lagattuta et al. 2019; Acebron et al. 2022), we also considered an external shear component to take into account possible perturbations due to the cluster environment and other non-modeled effects. We find that, while this model has comparable BIC and AIC values (173 and 106, respectively) to those of `LM-Model`, the RMS value of the former is significantly higher (0″.44), and equal in fact to that of the `WL-Model`.

In Fig. 5, we show the resulting total projected mass distribution of A2744 from our reference best-fit lens model superimposed to the HST/$F814W$ image. We find that adopting a different total mass parametrization of the cluster environment (i.e., `LM-Model` or `WL-Model`) results in consistent total projected mass values, with a median difference smaller than 3% in the region where multiple images are included in the modeling. We note that our lens model can be considered accurate up to
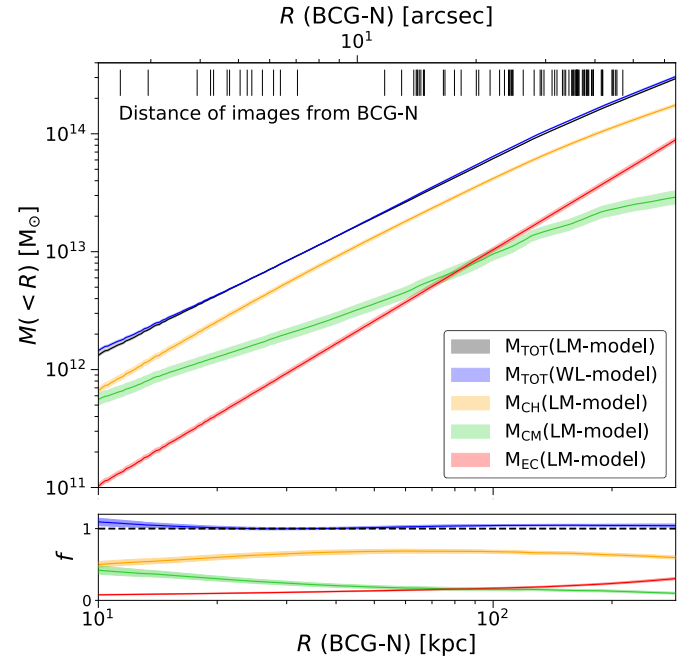
Fig. 7. Cumulative total mass profiles of the different mass components considered in the lens models. *Top*: cumulative total mass distribution of A2744 as a function of the projected distance R from BCG-N obtained from the reference lens model. The different components of the total mass are shown: cluster halo (CH), cluster members (CM, including the BCGs), and external clump (EC). The distances of the observed multiple images from BCG-N are plotted using small vertical bars. *Bottom*: ratio between the projected mass profiles obtained for the different color-coded mass components and the total cluster mass.

50–60″ from BCG-N (this is the largest distance at which secure multiple images have been identified). Model predictions outside that region are extrapolations and can, therefore, be prone to systematic errors.

Figure 7 shows the total projected cluster mass distribution within 300 kpc from BCG-N (in black), and its different components (as described in Eq. (4)). Due to the degeneracies between model parameters, a clear separation between the mass contributions from the BCGs and the cluster halo is not possible. The contribution of the member galaxies to the cluster total mass decreases as a function of the distance from the cluster center. At radii larger than 100 kpc, the mass contribution of the external clumps dominates over that of the subhalo. As shown in Table 1 and Fig. 5, the total mass contribution from the three external clumps is comparable to that of the main cluster halo. This result is also supported by previous weak lensing studies (Medezinski et al. 2016). In addition, the extended HST imaging reveals that the three brightest galaxies, associated with the three external clumps, have luminosity values comparable to those from BCG-N and BCG-S (the $F814W$ magnitude values of galaxies 1, 2, and 3 in Fig. 5 are in the range 18.1–18.2, compared to 18.3–18.4 for BCG-N and BCG-S). At a radius of 200 kpc, the total mass of the cluster is $M_{\text{tot}} = (1.77 \pm 0.07) \times 10^{14}\, M_\odot$, including both the statistical and systematic uncertainties (see Fig. 7).

In Fig. 4, we show the σ-luminosity relation for the member galaxies of A2744. For a proper comparison of the lensing velocity dispersion of the galaxies with the observed ones, the values are corrected for the spectroscopic aperture (0″.8), as detailed in Bergamini et al. (2019). The cluster member scaling relations
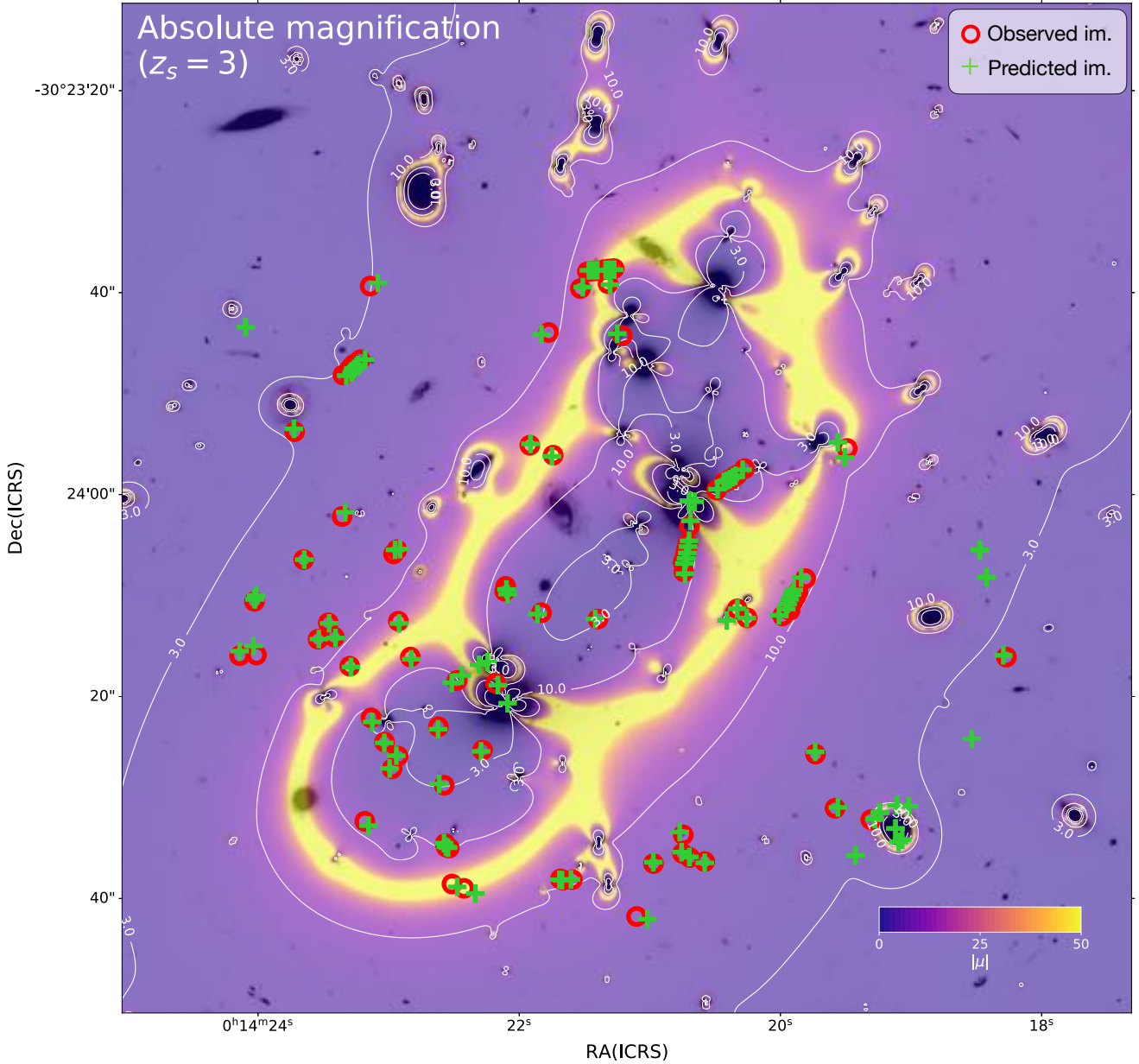
Fig. 8. Absolute magnification map computed for a source at redshift $z_s = 3$. Isomagnification contours for $|\mu|$ equal to 3.0 and 10.0 are plotted in white. The red circles indicated the observed positions of the 90 multiple images, while the green crosses show the predicted positions obtained with our best-fit `LM-model`.

inferred from the lens models are in excellent agreement with the kinematic results, although no prior on the $\sigma_{LT}^{\mathrm{ref}}$ value is assumed. We checked that by imposing a prior on that value, we found no significant difference in the Δ_{rms} value (i.e., $\sim0\farcs03$ higher). Our result highlights the importance of an independent determination and implementation of the subhalo velocity dispersion-luminosity scaling relation in parametric lens models, to reduce inherent model degeneracies between the cluster and galaxy-scale mass components.

In Fig. 8, we show the absolute magnification map computed for a background source at $z = 3$. While the magnification values are significantly different from one at large distances from the cluster center, we caution that these values are extrapolations in regions that lack SL constraints. Relatively large magnification values are also supported by the presence of several SL features that are visible at distances

between $\sim600-775$ kpc from BCG-N, revealed in the BUF-FALO imaging. The formation of these distant gravitational arcs is attributed to the presence of secondary cluster clumps surrounding A2744. As mentioned above, their total mass values are expected to be comparable to that of the main cluster (see Table 1).

5. SLOT: Strong Lensing Online Tool

The A2744 lens model presented in this work will be made publicly available with the publication of this paper. In order to allow interested users to access and exploit the model results, we have developed a graphical interface, pictured in Fig. 9. The Strong Lensing Online Tool, SLOT [4], will allow astronomers to take full

---

[4] SLOT is fully coded in python and mainly exploits the python package Panel (https://panel.holoviz.org/)
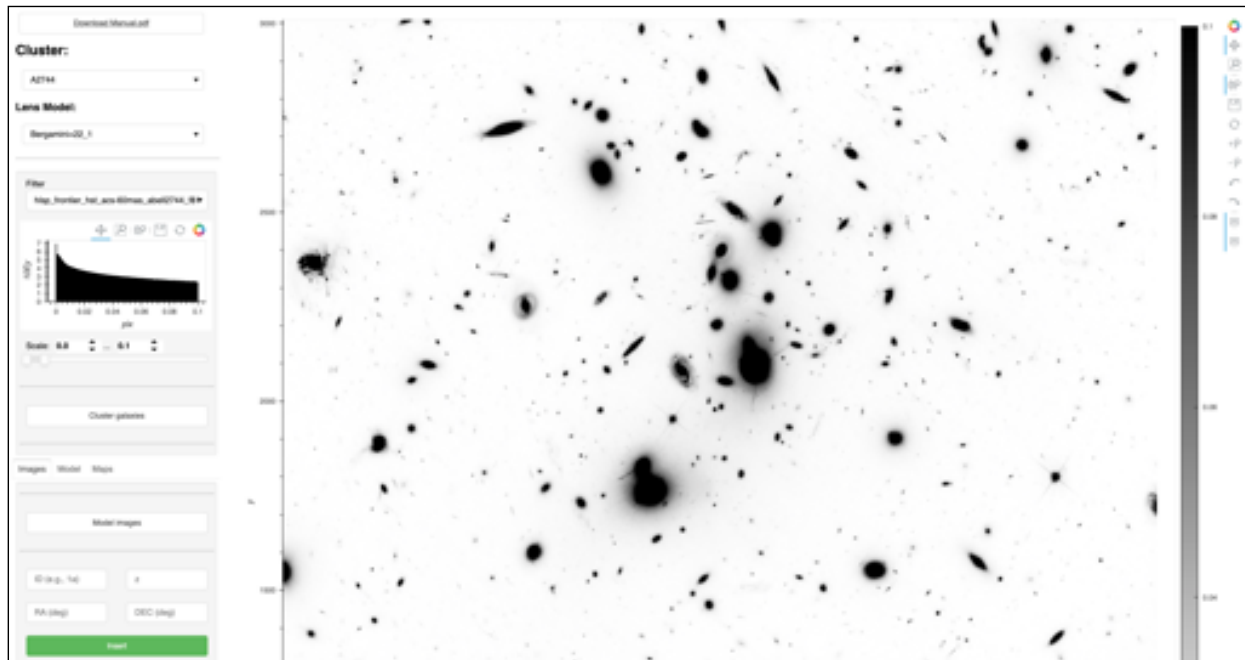
Fig. 9. The graphical interface of our new SLOT allows for full and easy access to high-level products, including the statistical uncertainties, of our lens models (`https://www.fe.infn.it/astro/lensing/`).

advantage of the predictive and statistical results of our high-precision SL model for their research, both for studies on cluster lenses and high-redshift sources. For example, `SLOT` can be used to: compute magnification values, with a careful estimation of the associated statistical errors, for all the sources in the field of A2744; obtain the predicted positions of the counter-images of every source defined by the user; derive and download maps, for example, of projected cluster total mass, deflection angle, and magnification. A description of the functionality of `SLOT` and the user manual can be found on the `SLOT` webpage.

6. Conclusions

We have presented a new high-precision SL model for the galaxy cluster A2744. A careful inspection of the HST and MUSE data allowed us to create a secure image data set counting 90 multiple images (from 30 background sources) whose point-like positions are used to constrain the lens model. This is currently the largest multiple image catalog compiled for this cluster. Our lens model also includes the information coming from the measured stellar kinematics of 85 member galaxies that is used to accurately characterize the subhalo component of the cluster. This component counts a total of 225 galaxies (including the two BCGs), 202 of which are spectroscopically confirmed cluster members. The gravitational lens A2744 is strongly affected by the presence of massive structures in the northwestern region of the cluster, at distances between $\sim600-775$ kpc from BCG-N. The contribution of these outer massive structures is taken into account by using three additional SIS profiles in our reference lens model fixed on the positions of the three brightest galaxies in that area.

The final $\Delta_{\rm rms}$ value of our reference model, `LM-model`, is equal to $0\farcs37$, representing a significant step forward with respect to previous SL models for the same cluster, and with the same data set (e.g., R21). The inclusion of the substructures within several extended sources as model constraints, including the radial arcs, allowed us to accurately characterize the inner total mass distribution of the cluster and the position of the clus-

ter critical lines. In addition, we found that accounting for the mass distribution of the cluster outside the core, particularly using the light of three prominent cluster galaxies as total mass tracers, is a key ingredient in order to accurately predict the positions of the multiple images.

Finally, we have presented a new publicly available graphical interface, called the Strong Lensing Online Tool (`SLOT`). Interested users, even non-lensing experts, can exploit the predictive power and the full statistical information of the lens model presented in this work through a user-friendly graphical interface.

We plan to apply our new high-precision SL model for the first analysis of the GLASS-JWST-ERS observations (see e.g., Vanzella et al. 2022), specifically to make use of magnification values and uncertainties for high-z lensed sources. Clearly, JWST imaging and spectroscopic data will reveal a larger number of multiply imaged sources with resolved substructures, over a more extended redshift range, which we will employ to improve the lens model presented in this work. In this context, our publicly available[5] lens model will be updated based on the latest available (e.g., JWST, MUSE) data.

---

[5] `https://www.fe.infn.it/astro/lensing/`

References

Acebron, A., Jullo, E., Limousin, M., et al. 2017, MNRAS, 470, 1809
Acebron, A., Grillo, C., Bergamini, P., et al. 2022, ApJ, 926, 86
Akaike, H. 1974, IEEE Trans. Autom. Control, 19, 716
Allen, S. W. 1998, MNRAS, 296, 392
Angora, G., Rosati, P., Brescia, M., et al. 2020, A&A, 643, A177
Annunziatella, M., Mercurio, A., Biviano, A., et al. 2016, A&A, 585, A160
Annunziatella, M., Bonamigo, M., Grillo, C., et al. 2017, ApJ, 851, 81
Bacon, R., Accardo, M., Adjali, L., et al. 2012, The Messenger, 147, 4
Bergamini, P., Rosati, P., Mercurio, A., et al. 2019, A&A, 631, A130
Bergamini, P., Rosati, P., Vanzella, E., et al. 2021a, A&A, 645, A140
Bergamini, P., Agnello, A., & Caminha, G. B. 2021b, A&A, 648, A123
Bonamigo, M., Grillo, C., Ettori, S., et al. 2017, ApJ, 842, 132
Bonamigo, M., Grillo, C., Ettori, S., et al. 2018, ApJ, 864, 98
Braglia, F. G., Pierini, D., Biviano, A., & Boehringer, H. 2009, VizieR Online Data Catalog: J/A+A/500/947
Caminha, G. B., Grillo, C., Rosati, P., et al. 2016, A&A, 587, A80
Caminha, G. B., Grillo, C., Rosati, P., et al. 2017a, A&A, 600, A90
Caminha, G. B., Grillo, C., Rosati, P., et al. 2017b, A&A, 607, A93
Caminha, G. B., Rosati, P., Grillo, C., et al. 2019, A&A, 632, A36
Cappellari, M. 2017, MNRAS, 466, 798
Cappellari, M., & Emsellem, E. 2004, PASP, 116, 138
Cerny, C., Sharon, K., Andrade-Santos, F., et al. 2018, ApJ, 859, 159
Coe, D., Zitrin, A., Carrasco, M., et al. 2013, ApJ, 762, 32
Coe, D., Salmon, B., Bradač, M., et al. 2019, ApJ, 884, 85
Couch, W. J., & Sharples, R. M. 1987, MNRAS, 229, 423
Diego, J. M., Molnar, S. M., Cerny, C., et al. 2020, ApJ, 904, 106
Diego, J. M., Pascale, M., Kavanagh, B. J., et al. 2022, A&A, 665, A134
Ebeling, H., Edge, A. C., Mantz, A., et al. 2010, MNRAS, 407, 83
Eckert, D., Jauzac, M., Shan, H., et al. 2015, Nature, 528, 105
Elíasdóttir, Á., Limousin, M., Richard, J., et al. 2007, ArXiv eprints [arXiv:0710.5636]
Giovannini, G., Tordi, M., & Feretti, L. 1999, New A, 4, 141
Girardi, M., & Mezzetti, M. 2001, ApJ, 548, 79
Govoni, F., Enßlin, T. A., Feretti, L., & Giovannini, G. 2001, A&A, 369, 441
Grillo, C., Suyu, S. H., Rosati, P., et al. 2015, ApJ, 800, 38
Grillo, C., Karman, W., Suyu, S. H., et al. 2016, ApJ, 822, 78
Grillo, C., Rosati, P., Suyu, S. H., et al. 2018, ApJ, 860, 94
Jauzac, M., Richard, J., Jullo, E., et al. 2015, MNRAS, 452, 1437
Jauzac, M., Eckert, D., Schwinn, J., et al. 2016, MNRAS, 463, 3876
Johnson, T. L., Sharon, K., Bayliss, M. B., et al. 2014, ApJ, 797, 48
Johnson, T. L., Rigby, J. R., Sharon, K., et al. 2017, ApJ, 843, L21
Jullo, E., & Kneib, J.-P. 2009, MNRAS, 395, 1319
Jullo, E., Kneib, J.-P., Limousin, M., et al. 2007, New J. Phys., 9, 447
Jullo, E., Natarajan, P., Kneib, J. P., et al. 2010, Science, 329, 924
Kempner, J. C., & David, L. P. 2004, MNRAS, 349, 385
Kneib, J.-P., Ellis, R. S., Smail, I., Couch, W. J., & Sharples, R. M. 1996, ApJ, 471, 643
Koekemoer, A. M., Avila, R. J., Hammer, D., et al. Am. Astron. Soc. Meeting Abstracts, 223, 254.02
Lagattuta, D. J., Richard, J., Bauer, F. E., et al. 2019, MNRAS, 485, 3738
Lam, D., Broadhurst, T., Diego, J. M., et al. 2014, ApJ, 797, 98
Limousin, M., Kneib, J.-P., & Natarajan, P. 2005, MNRAS, 356, 309
Limousin, M., Richard, J., Jullo, E., et al. 2016, A&A, 588, A99
Lotz, J. M., Koekemoer, A., Coe, D., et al. 2017, ApJ, 837, 97
Mahler, G., Richard, J., Clément, B., et al. 2018, MNRAS, 473, 663
Medezinski, E., Umetsu, K., Okabe, N., et al. 2016, ApJ, 817, 24
Meneghetti, M., Natarajan, P., Coe, D., et al. 2017, MNRAS, 472, 3177
Meneghetti, M., Davoli, G., Bergamini, P., et al. 2020, Science, 369, 1347
Meneghetti, M., Ragagnin, A., Borgani, S., et al. 2022, A&A, 668, A188
Mercurio, A., Rosati, P., Biviano, A., et al. 2021, A&A, 656, A147
Merten, J., Coe, D., Dupke, R., et al. 2011, MNRAS, 417, 333
Meštrić, U., Vanzella, E., Zanella, A., et al. 2022, MNRAS, 516, 3532
Montes, M. 2022, Nat. Astron., 6, 308
Owers, M. S., Randall, S. W., Nulsen, P. E. J., et al. 2011, ApJ, 728, 27
Pignataro, G. V., Bergamini, P., Meneghetti, M., et al. 2021, A&A, 655, A81
Postman, M., Coe, D., Benítez, N., et al. 2012, ApJS, 199, 25
Richard, J., Claeyssens, A., Lagattuta, D., et al. 2021, A&A, 646, A83
Schmidt, K. B., Treu, T., Brammer, G. B., et al. 2014, ApJ, 782, L36
Schwarz, G. 1978, Ann. Stat., 6, 461
Smail, I., Ellis, R. S., Dressler, A., et al. 1997, ApJ, 479, 70
Soto, K. T., Lilly, S. J., Bacon, R., Richard, J., & Conseil, S. 2016, MNRAS, 458, 3210
Steinhardt, C. L., Jauzac, M., Acebron, A., et al. 2020, ApJS, 247, 64
Treu, T., Schmidt, K. B., Brammer, G. B., et al. 2015, ApJ, 812, 114
Treu, T., Roberts-Borsani, G., Bradac, M., et al. 2022, ApJ, 935, 110
Vanzella, E., Caminha, G. B., Rosati, P., et al. 2021, A&A, 646, A57
Vanzella, E., Castellano, M., Bergamini, P., et al. 2022, A&A, 659, A2
Wang, X., Hoag, A., Huang, K. H., et al. 2015, ApJ, 811, 29
Weilbacher, P. M., Palsa, R., Streicher, O., et al. 2020, A&A, 641, A28
Zitrin, A., Zheng, W., Broadhurst, T., et al. 2014, ApJ, 793, L12

Appendix A: Multiple images

We present the catalog of the 90 secure multiple images (from 30 background sources) that are included as constraints in our SL model, and which represent the largest secure sample in the A2744 cluster field. All systems are discussed and are compared to the catalog presented in R21, in Sect. 3.1.

Table A.1. Catalog of the spectroscopic multiple images included in the SL modeling of A2744.

ID	R.A. deg	Decl deg	z_{spec}	QF	QP
1.1a	3.597561	-30.403925	1.688	3	1
1.1b	3.595963	-30.406808	1.688	2	1
1.1c	3.586226	-30.409986	1.688	3	1
1.2a	3.597072	-30.404723	1.688	3	1
1.2b	3.596395	-30.406143	1.688	3	1
1.2c	3.585748	-30.410100	1.688	3	1
1.3a†	3.597756	-30.403530	1.688	3	2
1.3b†	3.595528	-30.407199	1.688	3	2
1.3c†	3.586459	-30.409871	1.688	3	2
1.4a†	3.598082	-30.403980	1.688	1	1
1.4b†	3.595722	-30.407546	1.688	1	1
1.4c†	3.587383	-30.410152	1.688	1	1
2.1a	3.583265	-30.403339	1.887	3	1
2.1b	3.597289	-30.396712	1.887	3	1
2.1c	3.585369	-30.399878	1.887	3	1
2.1d	3.586412	-30.402127	1.887	3	1
2.2a†	3.583029	-30.403189	1.887	3	1
2.2b†	3.597138	-30.396639	1.887	3	1
2.2c†	3.585134	-30.399668	1.887	3	1
2.2d†	3.586438	-30.401870	1.887	3	1
2.3a†	3.582994	-30.403050	1.887	3	1
2.3b†	3.597095	-30.396580	1.887	3	1
2.3c†	3.585017	-30.399625	1.887	3	1
2.3d†	3.586394	-30.401765	1.887	3	1
2.4a†	3.582918	-30.402930	1.887	3	1
2.4b†	3.597052	-30.396527	1.887	3	1
2.4c†	3.584915	-30.399580	1.887	3	1
2.4d†	3.586353	-30.401632	1.887	3	1
2.5a†	3.582828	-30.402793	1.887	3	2
2.5b†	3.596990	-30.396469	1.887	3	2
2.5c†	3.584819	-30.399517	1.887	3	2
2.5d†	3.586322	-30.401490	1.887	3	1
2.6a†	3.582772	-30.402683	1.887	3	2
2.6b†	3.596942	-30.396421	1.887	3	2
2.6c†	3.584722	-30.399463	1.887	3	2
2.6d†	3.584719	-30.399462	1.887	3	2
2.7a†	3.582530	-30.402313	1.887	3	2
2.7b†	3.596734	-30.396291	1.887	3	2
2.7c†	3.584473	-30.399289	1.887	3	2
2.7d†	3.586236	-30.400869	1.887	3	2
3.1a†	3.588807	-30.393797	3.981	3	1
3.1b†	3.589375	-30.393857	3.981	3	1
3.2a†	3.589222	-30.393844	3.981	3	1
3.2b†	3.588965	-30.393815	3.981	3	1
3.3a	3.589487	-30.393869	3.981	3	1

Table A.1. continued.

ID	R.A. deg	Decl deg	z_{spec}	QF	QP
3.3b	3.588639	-30.393785	3.981	3	1
4.1a	3.592126	-30.402660	3.577	3	1
4.1b	3.595674	-30.401633	3.577	3	1
4.1c	3.580452	-30.408946	3.577	3	2
4.1e	3.593651	-30.405117	3.577	3	3
4.2a†	3.592098	-30.402527	3.577	3	1
4.2b†	3.595567	-30.401518	3.577	3	1
6.1a	3.598541	-30.401792	2.017	3	1
6.1b	3.594058	-30.407999	2.017	3	1
6.1c	3.586433	-30.409363	2.017	3	1
8.1a	3.589712	-30.394335	3.977	2	2
8.1b	3.588831	-30.394202	3.977	2	2
18.1a	3.576124	-30.404472	5.662	3	1
18.1b	3.588377	-30.395630	5.662	3	1
18.1c	3.590730	-30.395543	5.662	3	1
22.1a	3.587924	-30.411608	5.284	3	2
22.1b	3.600048	-30.404415	5.284	3	2
22.1c	3.596592	-30.408989	5.284	3	2
26.1a	3.593898	-30.409724	3.054	3	1
26.1b	3.590353	-30.410575	3.054	3	1
26.1c	3.600112	-30.402939	3.054	9	2
26.2a†	3.593993	-30.409699	3.054	3	1
26.2b†	3.590272	-30.410610	3.054	3	1
26.3a†	3.594031	-30.409604	3.054	2	3
26.3b†	3.589969	-30.410593	3.054	2	3
33.1a	3.584712	-30.403146	5.726	3	1
33.1b	3.584397	-30.403393	5.726	3	1
34.1a★	3.593428	-30.410834	3.784	2	1
34.1b★	3.593812	-30.410714	3.784	3	1
34.1c★	3.600711	-30.404593	3.784	2	1
42.1a	3.597313	-30.400605	3.692	3	1
42.1b	3.590956	-30.403252	3.692	3	1
42.1c	3.581590	-30.408631	3.692	3	1
42.1d	3.594245	-30.406388	3.692	3	1
42.1e	3.592415	-30.405197	3.692	1	3
61.1a	3.595522	-30.403485	2.951	1	1
61.1b	3.595138	-30.404471	2.951	3	1
62.1a	3.591326	-30.398643	4.194	3	3
62.1b	3.590582	-30.398918	4.194	3	3
63.1a	3.582214	-30.407142	5.662	3	1
63.1b	3.592836	-30.407032	5.662	3	2
63.1c	3.589153	-30.403427	5.662	3	1
63.1d	3.598830	-30.398273	5.662	3	1
64.1a	3.581203	-30.398734	3.409	3	1
64.1c	3.596420	-30.394264	3.409	3	1

Notes. † New families with respect to R21. ★ New position with respect to that adopted in R21

Appendix B: Cluster members

We present the catalog of the 225 cluster member galaxies that are included in our SL model, 202 of which are spectroscopically selected (based on the MUSE and ancillary spectroscopy, presented in Sect. 2.2) and 23 of which are identified based on HST multiband photometry through a CNN technique (see Sect. 3.2). The first two entries correspond to BCG-S and BCG-N, respectively.

Table B.1. Catalog of the spectroscopic (top) and photometric (bottom) cluster members included in the SL modeling of A2744.

ID	R.A. deg	Decl deg	m_{F160W}	z_{spec}
36034	3.592037	-30.405741	17.30	0.3185^a
37824	3.586257	-30.400172	17.34	0.2997^a
835	3.589290	-30.369074	16.88	0.3002^b
40689	3.594796	-30.391654	17.58	0.3006^a
736	3.575038	-30.428344	17.69	0.3170^b
938	3.610666	-30.395618	17.70	0.3033^b
814	3.587469	-30.371246	17.76	0.3038^b
947	3.612408	-30.409245	17.84	0.3031^b
34423	3.579662	-30.409189	17.84	0.3027^a
40059	3.585386	-30.394279	17.89	0.3202^a
783	3.583084	-30.433553	18.00	0.2927^b
20227	3.609542	-30.382110	18.03	0.3200^c
39382	3.587646	-30.396426	18.07	0.3031^a
36210	3.592510	-30.404611	18.24	0.3150^a
809	3.586500	-30.367380	18.29	0.3007^b
697	3.566354	-30.388260	18.40	0.3025^e
36527	3.578511	-30.403375	18.41	0.3155^a
38067	3.574900	-30.398381	18.46	0.3175^a
740	3.575081	-30.377074	18.49	0.3142^b
730	3.573503	-30.422861	18.50	0.3188^b
37947	3.592998	-30.399330	18.57	0.3092^a
834	3.589103	-30.419803	18.59	0.3044^b
894	3.602057	-30.377689	18.60	0.3011^b
41259	3.593289	-30.384378	18.60	0.2964^a
40592	3.589220	-30.389839	18.64	0.3151^a
41644	3.570173	-30.386449	18.66	0.2969^a
37954	3.586559	-30.399391	18.70	0.3229^a
35061	3.573945	-30.408829	18.71	0.3135^a
39428	3.588152	-30.395075	18.71	0.3002^a
41950	3.589184	-30.387396	18.72	0.3169^a
38907	3.585204	-30.394649	18.81	0.3009^a
642	3.556336	-30.387018	18.88	0.3115^b
38117	3.582159	-30.398571	18.89	0.2986^a
39072	3.598969	-30.397533	18.90	0.3162^a
41856	3.585314	-30.387545	18.91	0.3008^a
804	3.585629	-30.366902	18.98	0.2998^b
37344	3.604341	-30.400124	18.98	0.3190^a
41440	3.605429	-30.384843	18.99	0.3112^a
38010	3.588385	-30.398355	19.01	0.3173^a
678	3.562510	-30.402406	19.05	0.3025^b
38930	3.588680	-30.396077	19.07	0.3020^a
40243	3.580953	-30.390808	19.15	0.2931^a

Table B.1. continued.

ID	R.A. deg	Decl deg	m_{F160W}	z_{spec}
32284	3.602650	-30.416956	19.16	0.3132^a
690	3.565544	-30.387093	19.16	0.2991^b
40478	3.571507	-30.390436	19.18	0.2965^a
20018	3.581566	-30.376517	19.22	0.3130^c
902	3.604284	-30.414554	19.25	0.3061^b
966	3.618050	-30.403670	19.26	0.3115^b
42443	3.594708	-30.389115	19.26	0.3035^a
40314	3.590342	-30.390939	19.26	0.2972^a
720	3.571365	-30.422840	19.29	0.3030^b
41363	3.588146	-30.385006	19.30	0.2977^a
692	3.565347	-30.382948	19.38	0.3030^b
768	3.580711	-30.418875	19.39	0.2934^b
956	3.615142	-30.383729	19.41	0.3061^b
38729	3.578864	-30.397111	19.42	0.3190^a
973	3.618739	-30.392932	19.42	0.3015^b
36892	3.587938	-30.400852	19.44	0.3150^a
863	3.593561	-30.426049	19.46	0.2968^b
35339	3.595907	-30.406213	19.49	0.3161^a
950	3.613184	-30.389698	19.49	0.3026^b
20132	3.595399	-30.380404	19.50	0.3200^c
921	3.607012	-30.403478	19.51	0.2966^b
655	3.559037	-30.410659	19.51	0.2984^b
32547	3.601355	-30.415365	19.51	0.3197^a
37068	3.605266	-30.400808	19.52	0.3197^a
888	3.600962	-30.417843	19.59	0.3042^a
41418	3.592547	-30.385314	19.62	0.3164^a
931	3.609576	-30.378771	19.62	0.3009^b
39503	3.581389	-30.393932	19.63	0.2998^a
634	3.555379	-30.384632	19.66	0.3007^b
34556	3.591721	-30.407807	19.71	0.3194^a
816	3.587541	-30.373945	19.71	0.2963^b
961	3.616679	-30.402709	19.72	0.2943^b
41303	3.583714	-30.384680	19.75	0.3029^a
33910	3.589134	-30.409573	19.75	0.3173^a
42149	3.598764	-30.388018	19.76	0.3027^a
33540	3.588817	-30.410722	19.77	0.3223^a
787	3.583285	-30.432301	19.78	0.2942^b
39646	3.578948	-30.394119	19.80	0.3191^a
40884	3.590278	-30.382698	19.86	0.3019^a
37229	3.594463	-30.400350	19.89	0.3036^a
33328	3.569589	-30.412164	19.95	0.2990^a
40270	3.594239	-30.390462	19.97	0.3163^a
42269	3.595506	-30.388688	19.97	0.3032^a
13996	3.573450	-30.377932	20.00	0.3184^d
39710	3.584986	-30.392877	20.01	0.2954^a
35693	3.587039	-30.404948	20.04	0.2987^a
40551	3.589520	-30.389499	20.08	0.2939^a
21367	3.597859	-30.405556	20.12	0.3208^a
40832	3.588038	-30.382557	20.17	0.3116^a
39876	3.580373	-30.392204	20.21	0.2935^a
33699	3.582507	-30.409986	20.24	0.3188^a

Notes. ^{a}MUSE measurement from this work ^{b}Owers et al. (2011) ^{c}Treu et al. (2015), Schmidt et al. (2014) ^{d}Braglia et al. (2009) ^{e}Couch & Sharples (1987)

Table B.1. continued.

ID	R.A. deg	Decl deg	m_{F160W}	z_{spec}
38275	3.585521	-30.397156	20.24	0.3124^a
41655	3.573735	-30.385976	20.26	0.2965^a
41651	3.573383	-30.386313	20.34	0.3079^a
37230	3.583991	-30.399260	20.34	0.3200^a
40802	3.570861	-30.382004	20.37	0.3066^a
36220	3.605275	-30.402932	20.39	0.3161^a
39283	3.600830	-30.394896	20.39	0.3061^a
713	3.569303	-30.384236	20.42	0.2961^b
20089	3.597633	-30.379200	20.51	0.2800^c
32768	3.585709	-30.413971	20.59	0.3023^a
42195	3.578348	-30.387100	20.61	0.3076^a
13311	3.560070	-30.389342	20.61	0.2999^d
33870	3.595124	-30.409366	20.63	0.3199^a
35908	3.585035	-30.403315	20.63	0.3037^a
37609	3.578591	-30.399109	20.68	0.3054^a
36043	3.584377	-30.402887	20.83	0.3159^a
41908	3.604401	-30.384960	20.84	0.2962^a
34439	3.590280	-30.407401	20.92	0.3182^a
40032	3.593885	-30.390837	20.96	0.2970^a
36339	3.588145	-30.401980	20.97	0.2986^a
32088	3.603422	-30.416769	20.99	0.3179^a
38143	3.602200	-30.396988	21.01	0.3031^a
44545	3.578469	-30.381318	21.04	0.3179^a
36953	3.572810	-30.400534	21.05	0.3143^a
37825	3.602715	-30.397571	21.08	0.2990^a
40428	3.578347	-30.389464	21.12	0.2947^a
20064	3.577544	-30.378870	21.26	0.3080^c
36298	3.594832	-30.402130	21.30	0.3162^a
35576	3.587971	-30.404253	21.31	0.2998^a
40239	3.593166	-30.390349	21.33	0.3013^a
36849	3.596757	-30.400513	21.33	0.3167^a
34538	3.573400	-30.407461	21.46	0.3141^a
36843	3.579074	-30.400089	21.50	0.3056^a
40703	3.596256	-30.388517	21.54	0.2964^a
33671	3.583831	-30.409506	21.56	0.3023^a
33410	3.589721	-30.410222	21.57	0.3154^a
40708	3.571061	-30.388157	21.61	0.3032^a
38252	3.592874	-30.396356	21.61	0.2975^a
37214	3.585389	-30.399007	21.67	0.3006^8
36163	3.588499	-30.402102	21.70	0.2992^a
39727	3.584373	-30.391755	21.75	0.3200^a
41636	3.573693	-30.385685	21.79	0.2971^a
37542	3.584458	-30.398342	22.02	0.3235^a

Table B.1. continued.

ID	R.A. deg	Decl deg	m_{F160W}	z_{spec}
38175	3.583312	-30.396542	22.05	0.3073^a
35190	3.601244	-30.404885	22.11	0.3049^a
38267	3.597298	-30.396046	22.15	0.3189^a
33803	3.593740	-30.409224	22.18	0.3033^a
37367	3.601857	-30.398661	22.22	0.3144^a
42079	3.593478	-30.387595	22.24	0.2962^a
8024000	3.567362	-30.400881	22.30	0.3023^a
34705	3.594676	-30.405899	22.31	0.3072^a
41265	3.578737	-30.384233	22.33	0.3168^a
37199	3.603831	-30.399122	22.37	0.3026^a
41937	3.573015	-30.387260	22.43	0.3219^a
35514	3.574778	-30.403672	22.43	0.3039^a
32680	3.592097	-30.413109	22.45	0.3067^a
36814	3.593414	-30.400024	22.49	0.3040^a
36982	3.582898	-30.399701	22.49	0.2914^a
40944	3.593025	-30.382970	22.50	0.3005^a
37231	3.581618	-30.399105	22.51	0.3049^a
10440000	3.569048	-30.394963	22.56	0.3077^a
33503	3.597475	-30.409964	22.56	0.3051^a
10657000	3.569981	-30.394634	22.61	0.3011^a
41388	3.598749	-30.384458	22.61	0.3089^a
36872	3.595752	-30.399971	22.62	0.3160^a
34828	3.592717	-30.406107	22.65	0.3187^8
38459	3.572068	-30.395969	22.66	0.2990^a
39956	3.584993	-30.390870	22.67	0.3161^a
33933	3.585939	-30.408434	22.71	0.3080^a
41467	3.586832	-30.384627	22.74	0.3085^a
41842	3.591221	-30.386717	22.76	0.3132^a
38253	3.584471	-30.396056	22.78	0.3224^a
41531	3.589828	-30.385639	22.85	0.3174^a
4206000	3.600810	-30.409530	22.87	0.3068^a
36346	3.588851	-30.401771	22.89	0.3059^a
41930	3.608089	-30.387068	22.90	0.2962^a
33753	3.567161	-30.408755	22.92	0.3170^a
33911	3.577555	-30.408196	22.94	0.3068^a
39609	3.605171	-30.392616	22.98	0.3217^a
35436	3.589433	-30.404231	23.10	0.3184^a
4136000	3.590889	-30.410893	23.11	0.2983^a
41419	3.577521	-30.384813	23.12	0.3219^a
3476000	3.585092	-30.412314	23.13	0.3071^a
32671	3.588878	-30.413346	23.14	0.3047^a
35134	3.598182	-30.404825	23.15	0.3002^a

Table B.1. continued.

ID	R.A. deg	Decl deg	m_{F160W}	z_{spec}
38748	3.579869	-30.394391	23.15	0.3201[a]
12269000	3.577314	-30.390297	23.21	0.3131[a]
12325000	3.605930	-30.390167	23.24	0.3059[a]
38900	3.579626	-30.394091	23.26	0.3193[a]
42040	3.573600	-30.387182	23.27	0.2825[8]
10930000	3.572670	-30.393633	23.28	0.3198[a]
35978	3.596444	-30.403275	23.28	0.2989[a]
11577000	3.590109	-30.391576	23.31	0.3080[a]
36776	3.584729	-30.399826	23.33	0.3002[a]
3547000	3.566721	-30.411992	23.36	0.3002[a]
33468	3.595517	-30.409682	23.42	0.3219[a]
12191000	3.581882	-30.390474	23.44	0.3229[a]
37304	3.583931	-30.398595	23.45	0.2986[a]
40432	3.584083	-30.388909	23.46	0.2890[a]
34433	3.588518	-30.406316	23.47	0.3174[a]
5079000	3.586480	-30.407004	23.54	0.3199[a]
3795000	3.592497	-30.412103	23.55	0.3089[a]
10265000	3.597219	-30.395534	23.56	0.3196[a]
12018000	3.605043	-30.391671	23.64	0.2986[a]
8216000	3.597727	-30.400602	23.69	0.3155[a]
4938000	3.582862	-30.408838	23.70	0.3007[a]
35340	3.588510	-30.404209	23.73	0.3198[a]
7420000	3.568412	-30.402023	23.80	0.3054[a]
8330000	3.569485	-30.399955	23.83	0.3049[a]
14319	3.598659	-30.383098	23.38	–
15369	3.575794	-30.380405	23.72	–
9490	3.574867	-30.397183	23.80	–
10127	3.566005	-30.393924	21.12	–
12163	3.607988	-30.390726	23.14	–
14786	3.593635	-30.382101	23.16	–
5889	3.578093	-30.405740	23.76	–
15699	3.594368	-30.378664	22.52	–
15508	3.578849	-30.379423	23.88	–
7737	3.597161	-30.402246	23.97	–
13676	3.568877	-30.385314	20.36	–
15624	3.575140	-30.378524	21.58	–
5421	3.606797	-30.405592	20.39	–
14659	3.601322	-30.382501	23.43	–
2937	3.580614	-30.414102	22.85	–
15691	3.571676	-30.379704	23.55	–
9592	3.607186	-30.397230	23.56	–
2818	3.576712	-30.414622	23.56	–
16198	3.573701	-30.376807	22.99	–
5315	3.581605	-30.407436	23.58	–
3313	3.575661	-30.413496	23.61	–
15308	3.570284	-30.380798	23.64	–
14680	3.570831	-30.382935	23.67	–